















Constraints on Non-Thermal Pressure at galaxy cluster outskirts from a Joint SPT and XMM-Newton Analysis

ARNAB SARKAR ¹, MICHAEL McDONALD ¹, LINDSEY BLEEM ^{1,2,3}, MARK BAUTZ ¹, BRADFORD A. BENSON ^{4,3,5},
PRIYANKA CHAKRABORTY ⁶, CATHERINE E. GRANT ¹, CHRISTINE JONES ⁶, FLORIAN KÉRUZORÉ ⁷,
ERIC D. MILLER ¹, SCOTT RANDALL ⁶, CHARLES ROMERO ⁶, TAWEEWAT SOMBOONPANYAKUL ⁸ AND
YUANYUAN SU ⁹

¹*Kavli Institute for Astrophysics and Space Research, Massachusetts Institute of Technology, 70 Vassar St, Cambridge, MA 02139*

²*High-Energy Physics Division, Argonne National Laboratory, 9700 South Cass Avenue, Lemont, IL 60439, USA*

³*Kavli Institute for Cosmological Physics, University of Chicago, 5640 South Ellis Avenue, Chicago, IL 60637, USA*

⁴*Department of Astronomy and Astrophysics, University of Chicago, 5640 South Ellis Avenue, Chicago, IL 60637, USA*

⁵*Fermi National Accelerator Laboratory, P. O. Box 500, Batavia, IL 60510, USA*

⁶*Center for Astrophysics | Harvard & Smithsonian, Cambridge, MA 02138, USA*

⁷*Argonne National Laboratory 9700 S. Cass Avenue, Argonne, IL 60439-4815, United States*

⁸*Department of Physics, Faculty of Science, Chulalongkorn University, 254 Phayathai Road, Pathumwan, Bangkok 10330, Thailand*

⁹*University of Kentucky, 505 Rose street, Lexington, KY 40506, USA*

ABSTRACT

We present joint South Pole Telescope (SPT) and *XMM-Newton* observations of 8 massive galaxy clusters ($0.8\text{--}1.7\times 10^{15} M_{\odot}$) spanning a redshift range of 0.16 to 0.35. Employing a novel SZ+X-ray fitting technique, we effectively constrain the thermodynamic properties of these clusters out to the virial radius. The resulting best-fit electron density, deprojected temperature, and deprojected pressure profiles are in good agreement with previous observations of massive clusters. For the majority of the cluster sample (5 out of 8 clusters), the entropy profiles exhibit a self-similar behavior near the virial radius. We further derive hydrostatic mass, gas mass, and gas fraction profiles for all clusters up to the virial radius. Comparing the enclosed gas fraction profiles with the universal gas fraction profile, we obtain non-thermal pressure fraction profiles for our cluster sample at $>R_{500}$, demonstrating a steeper increase between R_{500} and R_{200} that is consistent with the hydrodynamical simulations. Our analysis yields non-thermal pressure fraction ranges of 8–28% (median: $15 \pm 11\%$) at R_{500} and 21–35% (median: $27 \pm 12\%$) at R_{200} . Notably, weak-lensing mass measurements are available for only four clusters in our sample, and our recovered total cluster masses, after accounting for non-thermal pressure, are consistent with these measurements.

Keywords: Galaxy cluster — ICM — Entropy — Cosmology

1. INTRODUCTION

Galaxy clusters, the largest gravitationally bound structures in the universe, offer a unique window into the complex interplay between dark matter, galaxies, and hot intracluster gas. Accurate estimation of cluster masses plays a crucial role in understanding the properties and dynamics of galaxy clusters (for review, Pratt et al. 2019). Traditionally, cluster mass estimates have been derived from X-ray and Sunyaev-Zel’dovich (SZ)

observations under the assumption that the intracluster medium (ICM) is in hydrostatic equilibrium with the gravitational potential of the cluster (e.g., Vikhlinin et al. 2006; Ettori et al. 2019; Sarkar et al. 2021). However, numerous studies have revealed inconsistencies between cluster mass estimates obtained through hydrostatic equilibrium and those derived from gravitational lensing measurements (e.g., von der Linden et al. 2014; Smith et al. 2016; Coe et al. 2019).

These inconsistencies, commonly known as hydrostatic mass bias, have raised questions about the validity of the hydrostatic equilibrium assumption and

have prompted investigations into the sources of such discrepancies (Barnes et al. 2021). It has been established that non-thermal pressure support in ICM, arising from processes such as turbulence, bulk motions, and magnetic fields, can significantly impact the estimation of cluster masses (e.g., Nagai et al. 2007; Kawaharada et al. 2010; Biffi et al. 2016; Shi et al. 2016; XRISM Collaboration 2025). The contribution from the magnetic field is negligible ($\lesssim 1\%$, Brunetti & Jones 2014), whereas the contribution from turbulence and bulk motion remains largely unknown. Although there is a spectroscopic confirmation of a low-level non-thermal pressure, for the Perseus Cluster using the *Hitomi* micro-calorimeter (Hitomi Collaboration et al. 2016), this measurement was limited to the cluster center. The micro-calorimeter onboard *XRISM* could provide crucial constraints on non-thermal pressure within R_{2500}^* (XRISM Science Team 2020). On the other hand, direct measurement of the non-thermal pressure support via line broadening using current X-ray high-resolution grating spectra is observationally expensive at larger radii of clusters. Future micro-calorimeter missions with large field of view, like LEM, will directly measure the spectral line broadening out to cluster outskirts (e.g., Kraft et al. 2022; Truong et al. 2023; Schellenberger et al. 2023).

In recent years, the combination of X-ray and SZ observations of clusters has emerged as a powerful approach to studying these cosmic giants (e.g., Ghirardini et al. 2018; Bulbul et al. 2019; Ruppin et al. 2021; Adam et al. 2015; Ruppin et al. 2017; Kéruszoré et al. 2020; Muñoz-Echeverría et al. 2023). In this letter, we explore the significance and potential of joint X-ray and SZ measurements in providing comprehensive insights into the physical processes governing galaxy clusters. These two observables, X-rays and SZ signals, probe different aspects of the cluster properties, enabling a multi-wavelength view of their structure and dynamics. The X-ray emission originates from the thermal bremsstrahlung of the hot ICM, providing information about its temperature, density, and metallicity (Chakraborty et al. 2020a,b; Sarkar et al. 2022a). On the other hand, the SZ effect, arising from the interaction of cosmic microwave background (CMB) photons with the energetic electrons in the cluster, offers a measure of the thermal energy and pressure of the ICM (Sunyaev & Zeldovich 1980).

In this letter, we present new results from our joint X-ray (*XMM-Newton*) and SZ (SPT) observations of a

sample of 8 galaxy clusters at redshift $0.16 < z < 0.35$. For the first time, we probe detailed thermodynamic profiles of clusters, including mass measurements, and account for the effects of non-thermal processes out to R_{200} and beyond in this redshift range. Previous studies using X-COP sample were limited to redshift < 0.1 , because of Planck’s large primary beam size ($\sim 10'$). Throughout this paper, we have adopted a cosmology of $H_0 = 70 \text{ km s}^{-1} \text{ Mpc}^{-1}$, $\Omega_\Lambda = 0.7$, and $\Omega_m = 0.3$. Unless otherwise stated, all reported error bars are at a 68% confidence level.

2. SAMPLE SELECTION AND DATA ANALYSIS

Our target selection criteria for this study include: (1) clusters with redshifts > 0.1 , (2) clusters are massive enough to be resolved by SPT ($M_{500} > 3 \times 10^{14} M_\odot$), and (3) clusters with modest *XMM-Newton* exposures of at least 30 ks. The chosen exposure time ensures enough photon counts to capture X-ray surface brightness profiles in smaller radial bins with reasonable 1σ uncertainty. For target selection, we focus on the 11 highest-luminosity REFLEX clusters at redshifts $z > 0.15$ studied by Plagge et al. (2010). These clusters, observable by the SPT due to a range of accessible elevation angles, were also observed by *XMM-Newton*. Out of these 11 clusters, RXCJ0217.2-5244 and RXCJ0528.9-3927 have *XMM-Newton* exposure times of ~ 20 ks and 13 ks, respectively. Despite having a ~ 58 ks *XMM-Newton* exposure, most observations of A3888 clusters suffer from high background levels. These three clusters are, therefore, not considered in this study. From the remaining clusters, we assemble a sample of 8 massive clusters within the redshift range $0.16 < z < 0.35$. This joint analysis aims to investigate the gas properties of these clusters and derive key physical parameters to understand the gas dynamics better. The details of our cluster sample are listed in Table 1.

2.1. SZ: South-Pole Telescope

The SPT is optimized for imaging large areas of the CMB sky with arcminute resolution, and one of its primary objectives is the identification of massive clusters via the SZ effect (Staniszewski et al. 2009). The galaxy clusters discussed in this work were observed using constant-elevation scans, where the telescope swept at a constant angular velocity in azimuth across the field and back while stepping in elevation and repeating the process. These observations were combined to create single maps for each field in different bands (Plagge et al. 2010; Bleem et al. 2022). For this work, we utilized the component-separated y -maps using a combination of data from the SPT-SZ and *Planck* (Bleem et al.

* R_Δ is radius from cluster core where matter density is Δ times the critical density of the Universe.

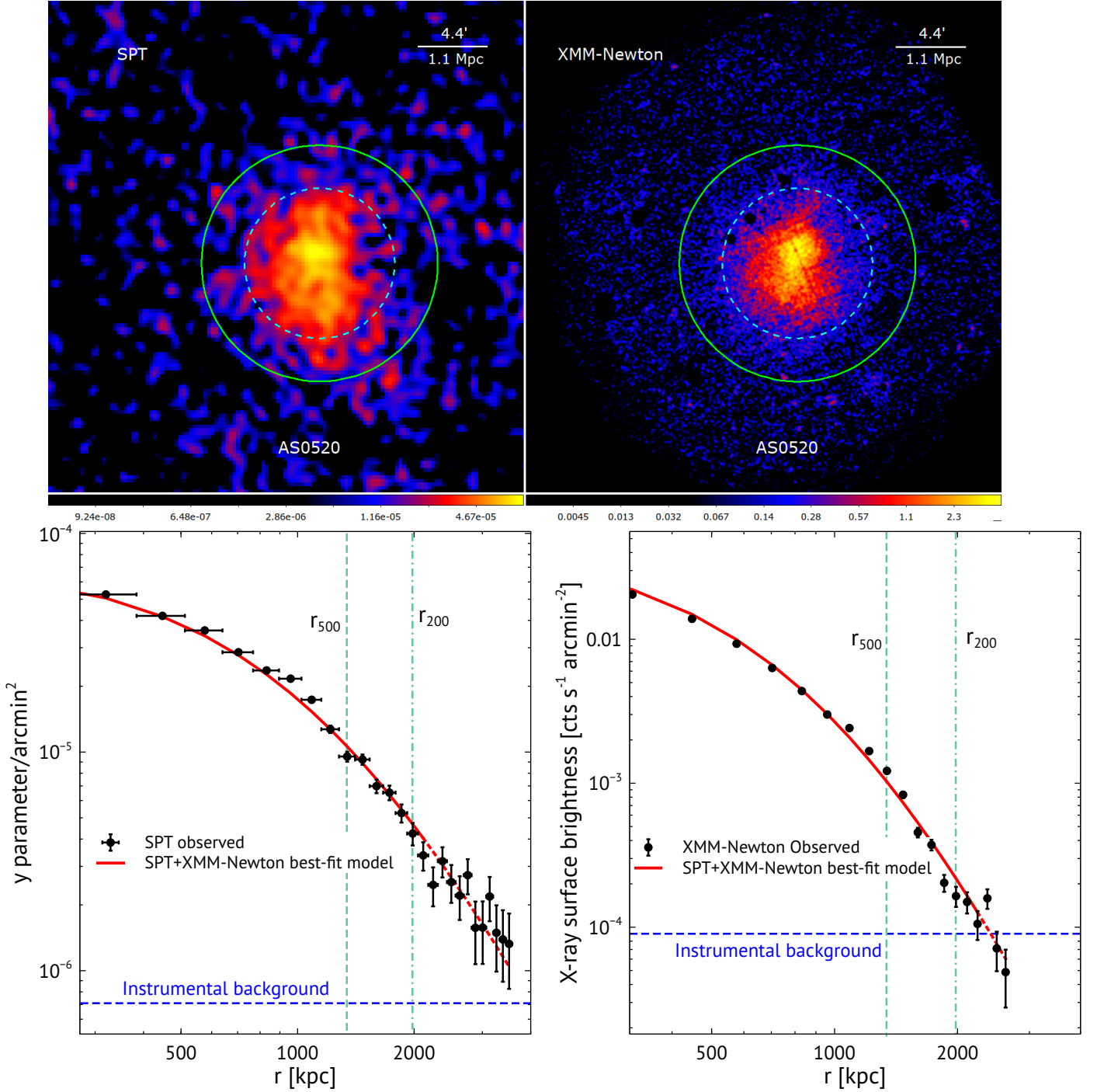


Figure 1. *Top Left:* SPT y -map of the galaxy cluster AS0520. *Top Right:* Quiescent particle-background subtracted X-ray counts image of AS0520 in the 0.7–1.2 keV energy band, obtained using *XMM-Newton*. The solid green and dashed cyan circles represent R_{200} and R_{500} , respectively, for AS0520. *Bottom Left:* y -parameter profile extracted from the SPT SZ map of AS0520. *Bottom Right:* Similar to the bottom left figure, but showing the X-ray surface brightness profile of AS0520 in 0.7–1.2 keV energy band. The surface brightness profile is exposure corrected and background subtracted. In both bottom panels, the best-fit curves, as shown in solid red, are obtained by fitting only in range $(0.15R_{500}–R_{200})$. We extended the best-fit curve, as shown in dashed red. Vertical dashed and dashed-dotted lines represent the R_{500} and R_{200} of AS0520, respectively. Horizontal blue dashed lines indicate respective instrumental background.

Cluster ID	RA	Dec	z	T_X (keV)	<i>XMM-Newton</i> exp. (ks)	R_{500}^a (Mpc)	SPT Data Source	Centroid shift*
A2744	0 ^h 14 ^m 18.6 ^s	-30°23′15.4″	0.307	10.1 ± 0.3 ^b	100	1.56	P10	-1.54 ± 0.01
A3404	6 ^h 45 ^m 30.0 ^s	-54°13′42.1″	0.164	8.1 ± 0.3 ^b	62	1.46	B22	-2.31 ± 0.04
AS0520	5 ^h 16 ^m 35.2 ^s	-54°30′36.8″	0.294	7.5 ± 0.3 ^b	67	1.34	B22	-1.37 ± 0.01
AS0592	6 ^h 38 ^m 46.5 ^s	-53°58′18.0″	0.222	8.0 ± 0.4 ^c	48	1.39	B22	-1.77 ± 0.02
AS1063	22 ^h 48 ^m 44.9 ^s	-44°31′44.4″	0.346	11.1 ± 1.1 ^d	52	1.44	P10	-1.76 ± 0.03
1ES 0657–56	6 ^h 58 ^m 30.2 ^s	-55°56′33.7″	0.297	10.6 ± 0.2 ^b	46	1.57	B22	-0.65 ± 0.01
RXCJ0232.2–4420	2 ^h 32 ^m 18.8 ^s	-44°20′51.9″	0.284	7.0 ± 0.3 ^b	40	1.25	B22	-2.89 ± 0.06
RXCJ2031.8–4037	20 ^h 31 ^m 51.5 ^s	-40°37′14.0″	0.342	10.9 ^e	30	1.2	B22	-1.31 ± 0.02

Table 1. Galaxy cluster sample adopted for this study. P10 and B22 are referred to [Plagge et al. \(2010\)](#) and [Bleem et al. \(2022\)](#), respectively. Cluster redshift is taken from [Plagge et al. \(2010\)](#). ^a radius measured from hydrostatic mass profiles. ^{b,c,d,e} Global X-ray temperatures taken from ([Zhang et al. 2006](#)), ([Hughes et al. 2009](#)), ([Maughan et al. 2008](#)), and ([Böhringer et al. 2004](#)), respectively. * Centroid shift is measured using XMM-Newton data and taken from [Yuan et al. \(2022\)](#).

2022), which are publicly available. These maps cover approximately 2500 square degrees of the southern sky with a $1.25'$ resolution and have been corrected for large-scale dust emissions and point sources. For our fiducial measurements, we utilized the minimum variance y -map presented in Bleem et al. (2022) due to its low noise and small beam size, which provides optimal sensitivity for our analysis.

We reprojected each y -map onto the tangent plane to analyze individual clusters in our sample, generating a 1024×1024 pixel cut-out y -map centered on each cluster's position and covering at least $20R_{200}$. Figure 1 (*top-left*) illustrates the resulting y -map for the AS0520 galaxy cluster as an example. For each cluster, we extracted the y -parameter radial profile from concentric annuli with $0.5'$ wide bins centered on each cluster core (X-ray centroid; Plagge et al. 2010). The radial range covered extends from the cluster center to $2R_{200}$. We accounted for the local background offset by selecting an area surrounding each cluster beyond $5R_{200}$. Since most of the clusters in our sample are relatively hot, we also accounted for relativistic corrections in the y -parameter profiles. Following Bleem et al. (2022), we applied a 5% correction for clusters with $T_X \leq 10$ keV and an 8% correction for clusters with $T_X > 10$ keV. The statistical uncertainties of the y -parameters were estimated by performing random sampling of y -maps in source-free regions. Figure 1 (*bottom-left*) shows the resulting y -parameter profile for the cluster AS0520.

For further details regarding the construction, algorithms, and validation of the maps used in this analysis, we refer the readers to Bleem et al. (2022).

2.2. X-ray: XMM-Newton

We used archival XMM-Newton-EPIC data spanning over two decades for those 8 galaxy clusters. The data analysis for this study was performed using the XMM-Newton Extended Source Analysis Software (XMM-ESAS[†]) and related methods to process the EPIC (European Photon Imaging Camera) data. Initially, the event files were subjected to basic filtering and calibration using XMM-ESAS tools, including `epchain`, `emchain`, `mos-filter`, and `pn-filter`. These tools applied the latest XMM-ESAS Current Calibration Files database to ensure accurate data calibration and removed flares using the unexposed corners of the instrument, using a high-energy band from 2.5 keV to 12 keV.

[†] <https://heasarc.gsfc.nasa.gov/docs/xmm/abc/>

The images were created in the 0.7-1.2 keV energy band from the filtered event files and used to detect point sources. Exposure maps were also created for each detector to account for chip gaps and mirror vignetting. The automated point-source detection task `cheese-bands` within XMM-ESAS was utilized to detect point sources. All these point sources were excluded from further analysis. The quiescent particle background (QPB) images were created from filter-wheel closed data by employing `mos-back` and `pn-back` tools (Snowden et al. 2008).

Figure 1 (*top-right*) shows the resulting point source excluded, and QPB subtracted count image of AS0520. The local sky background were estimated from a region surrounding each cluster beyond R_{200} . Some of the clusters in our sample are undergoing mergers, with substructures present within the central region. We cut out the regions obviously contaminated by substructures from the X-ray image, before extracting surface brightness profiles. Finally, we extracted sky + particle background removed X-ray surface brightness profiles for each cluster from the similar annuli bins used for y -parameter profiles, as shown in Figure 1 (*bottom-right*). We adopted median technique as proposed by Eckert et al. (2015) to extract X-ray surface brightness profiles to avoid biases in 3D density profiles due to presence of gas clumping at cluster outskirts.

The dynamical state of galaxy clusters is commonly characterized by their proximity to virial equilibrium at a given time, as this can influence the measurement of non-thermal pressure and, consequently, the estimation of cluster masses (e.g., Nelson et al. 2012; Biffi et al. 2016). In this study, we employ the centroid shift as an indicator of dynamical state. The centroid shift values for our cluster sample were adopted from Yuan et al. (2022), who analyzed XMM-Newton observations of 1,308 galaxy clusters.

3. JOINT SZ AND X-RAY ANALYSIS

For each cluster in our sample, we utilize the above described SZ y -parameter and X-ray surface brightness profiles to measure the thermodynamic profiles out to R_{200} and beyond.

3.1. Density and temperature profiles

SZ observations directly measure the dimensionless Comptonization parameter, y , which represents the strength of interaction between CMB photons and the ICM electrons. This Compton- y parameter provides the measurement of thermal pressure integrated along the line of sight (Sunyaev & Zeldovich 1972),

$$y = \frac{\sigma_T}{m_e c^2} \int P dl, \quad (1)$$

where l is the distance along the line of sight, σ_T is the Thompson scattering cross-section, m_e is the electron mass, and c is the speed of light. Thermal gas pressure, P , in Equation 1 can be described as

$$P = k_B n_e T_e, \quad (2)$$

where n_e , T_e , and k_B are the gas density, temperature, and the Boltzmann constant, respectively.

On the other hand, *XMM-Newton* observations provide the X-ray surface brightness of ICM, which is a function of gas density and temperature (Sarazin 1988),

$$S_X \approx \int n_e^2 T_e^{1/2} dl, \quad (3)$$

where the integration is along the line of sight. One can use parametric expressions of n_e and T_e in Equations 1, 2, and 3 and fit y -parameter and X-ray surface brightness profiles simultaneously to put tighter constraints on n_e and T_e (see Ruppin et al. 2021). We follow this prescription for each of the clusters in our sample. We note that temperature dependence in Equation 3 is relatively mild due to the use of narrow X-ray band. We adopt a gNFW density model, as described in Amodeo et al. (2021),

$$n_e(r) = \frac{n_0}{(c_{500}x)^\gamma [1 + (c_{500}x)^\alpha]^{\frac{\beta-\gamma}{\alpha}}}, \quad (4)$$

where $x = r/R_{500}$, c_{500} is the concentration parameter and γ , α , β are the slopes at $r \ll r_s$, $r \sim r_s$, and $r \gg r_s$, respectively, r_s is a scale parameter $r_s = R_{500}/c_{500}$.

For temperature, we adopt a universal temperature profile as described in Loken et al. (2002),

$$T_e(r) = T_0 [1 + r/r_c]^{-\delta}, \quad (5)$$

where T_0 , r_c , and δ are free parameters. For each cluster in our sample, we employ the aforementioned expressions for density and temperature in Equations 1 to 3 and simultaneously fit the y -parameter and X-ray surface brightness profiles. The parameters n_0 , r_s , α , β , γ , T_0 , r_c , and δ in Equations 4 and 5 are allowed to vary freely during the fitting process. We emphasize that the above temperature profile model accurately characterizes the gas temperature of the ICM at the larger radii (specifically, $\gtrsim 0.15R_{500}$). However, it is important to note that this model does not provide constraints on temperature variations within the central region ($< 0.15R_{500}$). We, therefore, restrict our fitting process within $0.15R_{500} < r < R_{200}$. We note that this limitation does not affect the outcomes of our study since our primary focus is to derive non-thermal pressure at larger radii (between R_{500} and R_{200}).

It's important to highlight that we opted not to adopt the well-known density and temperature profiles by Vikhlinin et al. (2006). These profiles involve 10 free parameters for density and 9 for temperature. Given the context of our SZ + X-ray joint analysis, encompassing simultaneous projection and fitting with 19 free parameters, the computational complexity becomes formidable, and the statistical significance is limited. Our approach with 8 free parameters provides sufficient functional freedom for the fitting process and better matches the constraining power of the data. The resulting best-fit parameters are listed in Table B.

The uncertainties are estimated using the affine invariant Markov Chain Monte Carlo (MCMC) sampler implemented in the *emcee* package by Foreman-Mackey et al. (2013). To illustrate the results, Figure 1 (*bottom* panels) displays the best-fit y -parameter and X-ray surface brightness profiles for cluster AS0520 as an example. This procedure is repeated for all 8 clusters in our sample. The resulting best-fit scaled density and deprojected temperature profiles are presented in Figure 2 (*top* panel). Temperature profiles are scaled by R_{500} and T_{500} , where T_{500} is

$$T_{500} = 8.85 \text{ keV} \left(\frac{M_{500}}{h^{-1} 10^{15} M_\odot} \right) E(z)^{2/3} \left(\frac{\mu}{0.6} \right), \quad (6)$$

where M_{500} and $\mu \sim 0.6$ are hydrostatic mass at R_{500} (measured from hydrostatic mass profiles shown in Figure 3) and mean molecular weight. $E(z)$ can be expressed as $E(z) = \sqrt{\Omega_m (1+z)^3 + \Omega_\Lambda}$.

Our results show that the density profiles decline dramatically by ~ 2 dex from center ($> 0.15R_{500}$) to outskirts, consistent with the previous observations, such as the X-COP sample (Ghirardini et al. 2019) and $z > 0.3$ SPT clusters (Ruppin et al. 2021). In contrast, the deprojected temperatures experience relatively mild variations across the same radial span. Similar temperature variations can also be seen in the X-COP sample (Ghirardini et al. 2019) and in $z > 1.2$ SPT clusters (Ghirardini et al. 2021). We also derive the global temperatures of the clusters in our sample by projecting the best-fit temperature profiles onto the sky plane, as discussed in Appendix C. We then compare our results with global temperatures obtained from spectral fits using Chandra and XMM-Newton observations. Our X-ray+SZ measurements more closely align with the temperatures measured by XMM-Newton, as shown in Figure 6.

3.2. Pressure and entropy profiles

If the ICM is unaffected by any ongoing merger, gas pressure typically exhibits the smoothest thermo-

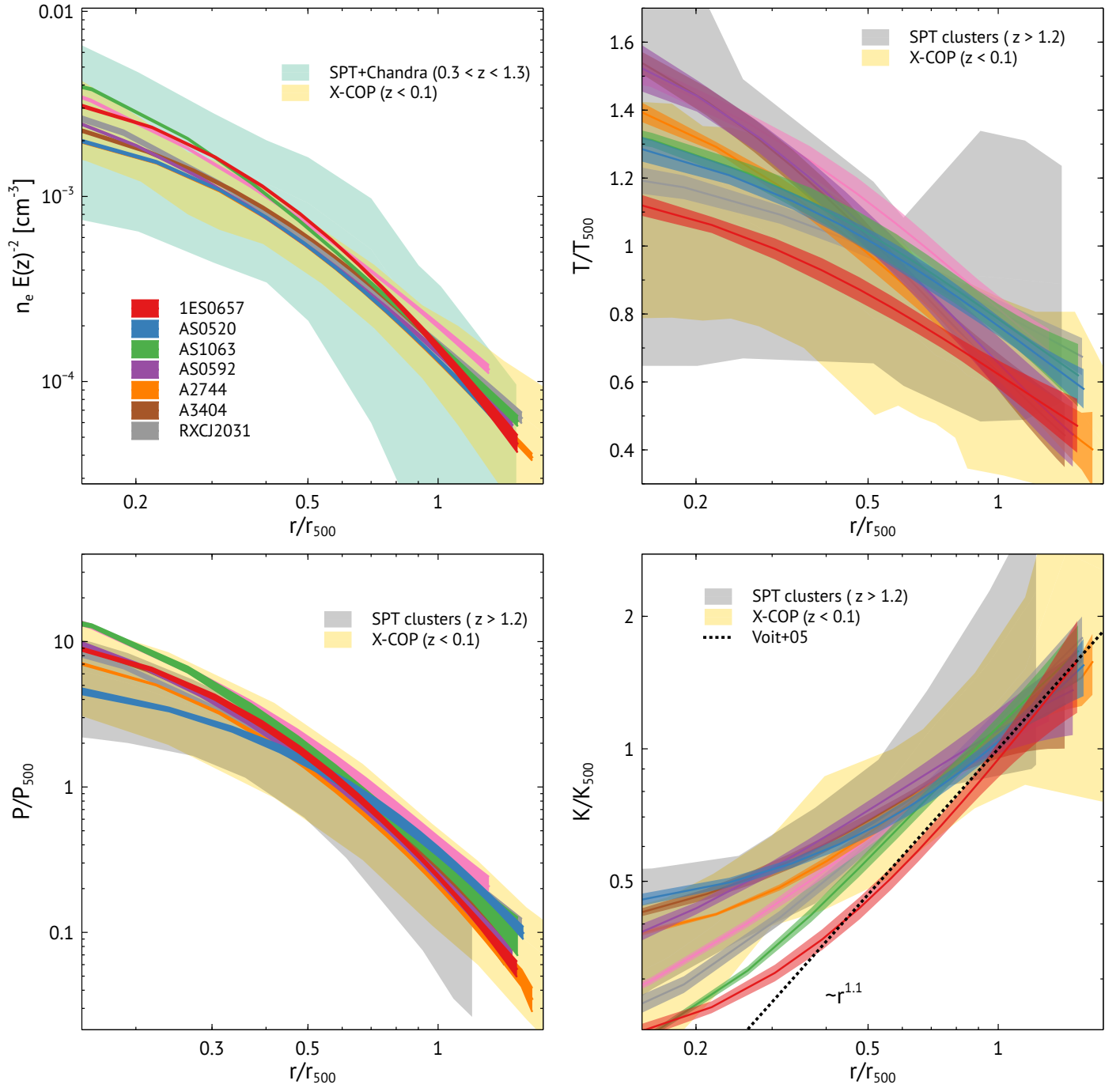


Figure 2. Best-fit gas properties of galaxy clusters in our sample. *Top-Left:* shows the scaled best-fit electron density profiles. Green shade represents density profiles of 67 high-redshift SPT clusters within ($0.3 < z < 1.3$) (Ruppin et al. 2021). *Top-Right:* scaled best-fit deprojected temperature profiles. *Bottom-Left:* scaled deprojected pressure profiles. *Bottom-Right:* scaled entropy profiles. Dotted line shows self-similar entropy profile (Voit et al. 2005). In all panels, yellow shaded regions represent gas properties for X-COP sample of cluster with redshift $z < 0.1$ (Ghirardini et al. 2019). In top-right, bottom-left, and bottom-right panels, black shade regions shows the gas properties of high-redshift ($z > 1.2$) SPT clusters (Ghirardini et al. 2021).

dynamic quantity along the azimuth. We derive the deprojected pressure profiles for our cluster sample from Equation 2 by employing best-fit density and deprojected temperature profiles. Pressure profiles are scaled by R_{500} and P_{500} , where P_{500} is

$$P_{500} = 3.426 \times 10^{-3} \text{ keV cm}^{-3} \left(\frac{M_{500}}{h^{-1} 10^{15} M_{\odot}} \right) E(z)^{8/3} \left(\frac{\mu}{0.6} \right). \quad (7)$$

Figure 2 (*bottom-left*) shows the deprojected pressure profiles of our cluster sample. We compare our measurements with that of the low-redshift X-COP sample (Ghirardini et al. 2019) and high-redshift ($z > 1.2$) SPT clusters (Ghirardini et al. 2021), as shown in Figure 2. Our results are consistent with those previous studies, except for AS1063 and RXCJ2032 in the central region.

Entropy, a critical parameter that depends on the gas temperature (kT) and electron density (n_e) as $K = kT/n_e^{2/3}$, plays a crucial role in understanding the thermal history of ICM. By examining the entropy as a function of radius, we can trace the thermal evolution of the ICM plasma, which is subject to various processes such as cooling/heating, mixing, and convection (see Walker et al. 2019, for review).

Numerical simulations focusing on gravity-only structure formation (Voit et al. 2005) have shown entropy increases radially from the cluster center, following a power law. These simulations provide a baseline entropy profile prediction when clusters are scaled by the self-similar entropy K_{500} , resulting in the expression $K(r)/K_{500} \approx (r/R_{500})^{1.1}$. K_{500} can be expressed as,

$$K_{500} = 1667 \left(\frac{M_{500}}{h_{70}^{-1} 10^{15} M_{\odot}} \right)^{2/3} E(z)^{-2/3} \text{ keV cm}^2 \quad (8)$$

Deviation from this baseline entropy profile indicates the presence of non-gravitational physics (see Nagai & Lau 2011; Akamatsu et al. 2011, for review). In this study, we derived the entropy profiles of our cluster sample extended to R_{200} and beyond, as shown in Figure 2 (*bottom-right*). We find that the majority (5 out of 8) of the clusters exhibit a good agreement with the baseline entropy profile between R_{500} and R_{200} , suggesting that gravitational physics predominantly governs the thermal evolution in this radial range. However, when examining individual clusters, we note that both A2744 and AS0592 display mild entropy flattening at R_{200} , although their upper limits of 1σ errorbar remain consistent with the baseline profile. In contrast, A3404 exhibits a significant entropy flattening that deviates from the baseline profile beyond the uncertainties. Our measured density profiles are free from potential clumpy gas at the outskirts since we derive it from median surface brightness profiles (Ghirardini et al. 2019).

This implies thermal non-equilibrium between electrons and ions and/or large scale inhomogeneities of cluster gas distribution may contributing to the entropy flattening near the virial radius.

Furthermore, the central regions ($< R_{500}$) of our cluster sample show higher entropy values compared to the baseline profile. This discrepancy partly suggests that non-gravitational physics, specifically related to cooling, AGN feedback, and merging events, play a substantial role in increasing the entropy (Sarkar et al. 2022b, 2023; Ayromlou et al. 2023). Our findings are consistent with the previous studies (e.g., Pratt et al. 2010; Cavagnolo et al. 2009), indicating that central heating and mixing mechanisms significantly influence the gas properties of galaxy clusters. We also find our results are consistent with that of X-COP and $z > 1.2$ SPT clusters for the entire radial range considered, as seen in Figure 2 (*bottom-right*).

3.3. Mass and f_{gas} profiles

Under the assumption of the spherically symmetric distribution of the ICM and adherence to the equation of state for an ideal gas, the combined information of gas density and pressure enables the estimation of the total mass of a cluster within a given radius (Sarazin 1988). This estimation can be achieved through the hydrostatic equilibrium equation, which accounts for the gravitational force acting on the gas. We assume the ICM is in hydrostatic equilibrium (HSE) within the potential well, with the kinetic energy converted entirely into thermal energy (Ettori et al. 2019). In this case, hydrostatic mass within a given radius (r) can be written as

$$M_{\text{HSE}}(< r) = - \frac{r^2}{\rho_{\text{gas}} G} \frac{dP_{\text{th}}}{dr}, \quad (9)$$

where P_{th} is the thermal electron pressure. $\rho_{\text{gas}} = 1.92 \mu m_p n_e$ is the gas density (Su et al. 2015).

In this study, we use deprojected pressure and best-fit electron density profiles obtained from joint SZ and X-ray fitting. These profiles are then used to solve Equation 9 to estimate the hydrostatic mass for our sample of clusters. Figure 3 (*top-left*) presents the resulting hydrostatic mass profiles for the cluster sample, spanning from the central region to the outskirts. These profiles offer insights into the distribution of mass within the clusters. The high statistical quality of the SPT and *XMM-Newton* data and our novel joint fitting technique results in overall measurement uncertainties of $\sim 5\%$ for hydrostatic mass within R_{200} .

We also derive ICM gas mass within a given radius (r) by integrating the best-fit gas density profile,

$$M_{\text{gas}}(< r) = 4\pi \int_0^r \rho_{\text{gas}}(r') r'^2 dr', \quad (10)$$

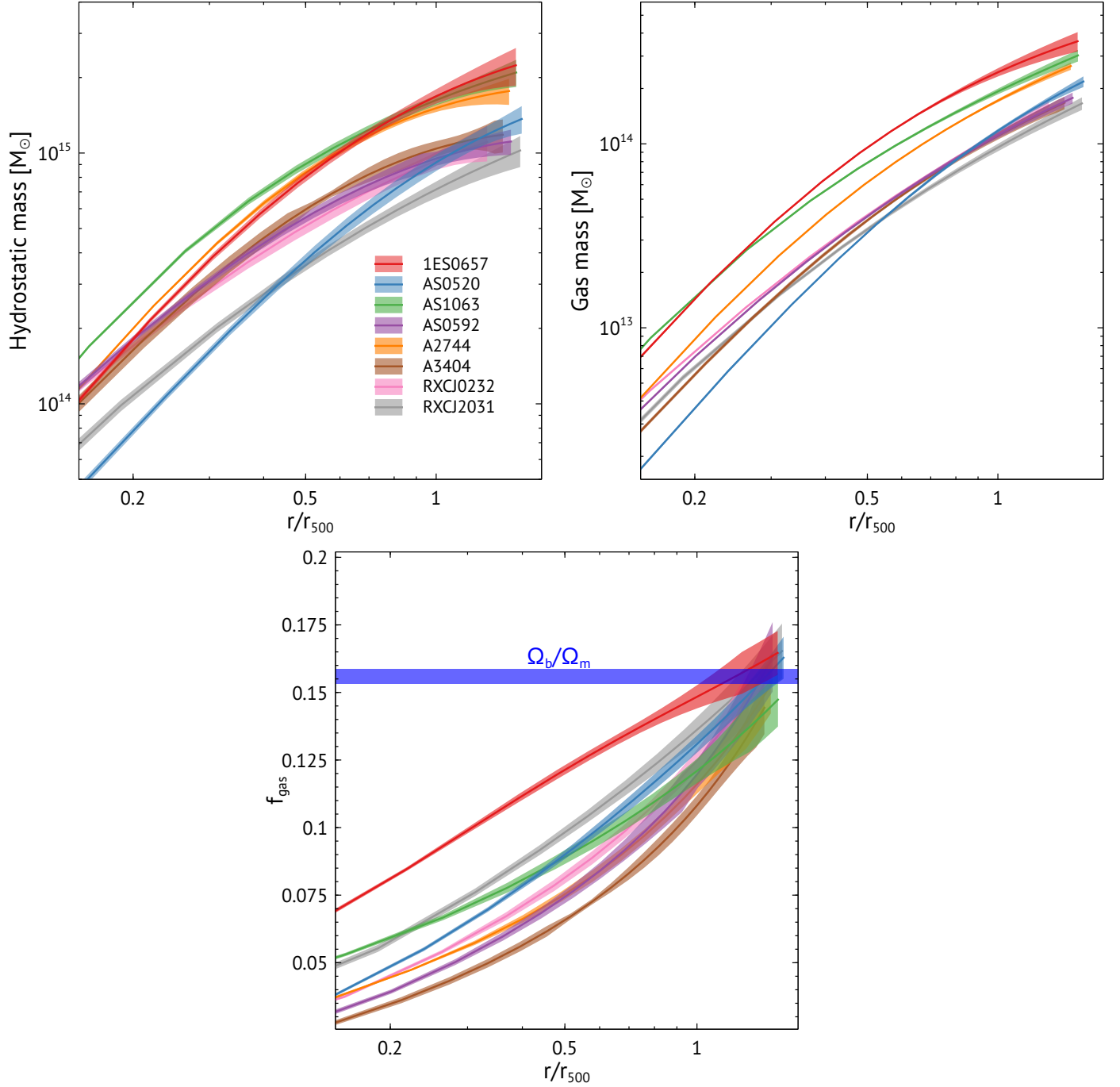


Figure 3. *Top-Left:* hydrostatic mass profiles of the clusters derived using best-fit pressure and density profiles and assuming hydrostatic equilibrium. *Top-Right:* gas mass profiles of the sample of clusters using best-fit density profiles and assuming a spherical geometry. *Bottom Left:* the gas mass fraction profiles of the sample of clusters. Blue horizontal shaded region shows the *Planck* universal baryon fraction Ω_b/Ω_m (Planck Collaboration et al. 2016).

assuming spherical symmetry for the clusters. Figure 3 (*top-right*) shows the gas mass profiles for all 8 clusters in our sample. To further characterize the gas content within the clusters, we compute the enclosed gas fraction profiles, defined as $f_{\text{gas,HSE}}(< r) = M_{\text{gas}}(< r)/M_{\text{HSE}}(< r)$. The gas fraction profile quantifies the fraction of the total mass composed of ICM gas and provides valuable information regarding the baryonic content of the clusters.

In Figure 3 (*bottom*), we display the enclosed gas fraction profiles of our cluster sample as a function of the scaled radius. These profiles allow us to explore the variations in gas fraction across different cluster scales and provide insights into the distribution of baryonic matter (Pratt et al. 2010). It is important to note that the radial range of each profile corresponds to regions where reliable information on density and pressure is available, ensuring robust estimates of the gas fraction. For our cluster sample, we are able to measure hydrostatic mass, gas mass, and hence gas fraction profiles out to $\gtrsim R_{200}$ without requiring any extrapolation. Throughout our analysis, we have accounted for statistical uncertainties. The typical uncertainties in $f_{\text{gas,HSE}}$ are approximately $\leq 5\%$ at R_{500} and approximately $\leq 10\%$ at R_{200} , reflecting the precision of our measurements and the reliability of the SZ + X-ray joint fitting technique for such high-redshift clusters. We note that our SPT + *XMM-Newton* fitting process may under-estimate the uncertainties reported here due to our choice of simple temperature model.

4. NON-THERMAL PRESSURE SUPPORT

Quantifying the magnitude of non-thermal pressure contribution is imperative for understanding the mechanisms driving the virialization of the gas confined within the gravitational potential of the halo, as well as for accurately calibrating biases inherent in hydrostatic mass estimations (Nelson et al. 2014). Despite the importance, the observational constraints on non-thermal pressure at larger radii ($>0.5R_{500}$) of high-redshift clusters are still largely unknown. We, therefore, examine the non-thermal pressure support in the ICM of our cluster sample.

4.1. Universal gas fraction

The universal gas fraction within a given radius can be written as

$$f_{\text{gas,univ}}(r) = Y_b(r) \frac{\Omega_b}{\Omega_m} - f_\star, \quad (11)$$

where Y_b and f_\star are baryon depletion factor and fraction of baryons converted into stars (or stellar fraction),

respectively. Baryon depletion factor and stellar fraction have been extensively studied in the literature (e.g., Kravtsov et al. 2005; Planelles et al. 2013; Rasia et al. 2015; Ayromlou et al. 2023). In this present work, we adopt the baryon depletion factor and stellar fraction profiles predicted by Angelinelli et al. (2022) for a wide mass range, using Magneticum cosmological simulation. Their selected sub-sample of galaxy clusters has an average redshift of $z = 0.25$, consistent with the median redshift value $z = 0.29 \pm 0.06$ of our cluster sample. For this work, we specifically use baryon depletion factor and stellar fraction profiles of halos with mass $> 5.4 \times 10^{14} h^{-1} M_\odot$, since our sample consists of most massive clusters with $M_{500} > 5 \times 10^{14} M_\odot$ (see Figure 3). Finally, we estimate the universal gas fraction profile using Equation 11 in the $0.5 - 2R_{500}$ radial range. We adopt $\Omega_b/\Omega_m = 0.156$ (Planck Collaboration et al. 2016). Figure 4 shows the baryon depletion factor, stellar fraction, and resulting universal gas fraction profiles considered in this work. We use $R_{500} < r < 2R_{500}$ radial range of Y_b and f_\star profiles for non-thermal pressure measurements (Sembolini et al. 2016).

4.2. Non-thermal pressure fraction

Accurate estimation of cluster masses from X-ray and SZ observations relies on the fundamental assumption that ICM is in hydrostatic equilibrium with the gravitational potential of the cluster. However, previous studies have highlighted discrepancies between the mass estimates obtained through hydrostatic equilibrium and those derived from gravitational lensing measurements (Mahdavi et al. 2013; von der Linden et al. 2014; Nelson et al. 2014). This hydrostatic mass bias is attributed to the non-thermal pressure support within the galaxy clusters. Unfortunately, direct measurement of this non-thermal pressure using X-ray CCD/grating spectra of the ICM poses significant challenges and becomes increasingly unfeasible at larger radii. To address this issue, we adopt a methodology similar to that employed by Nelson et al. (2014) to estimate the non-thermal pressure support for our cluster sample.

In the presence of isotropic non-thermal pressure, the hydrostatic equilibrium equation can be modified as -

$$\frac{d}{dr} [P_{\text{th}}(r) + P_{\text{NT}}(r)] = -\rho_{\text{gas}} \frac{GM_{\text{tot}}(< r)}{r^2}, \quad (12)$$

where P_{th} and P_{NT} are the thermal and non-thermal pressure, respectively, and $M_{\text{tot}}(< r)$ is the true total mass of a cluster within a given radius r . The non-thermal pressure fraction, $\alpha(r)$, can be defined as the ratio between non-thermal pressure and total pressure, $\alpha(r) = \frac{P_{\text{NT}}}{P_{\text{th}} + P_{\text{NT}}}$. Together with $\alpha(r)$ and Equation 9,

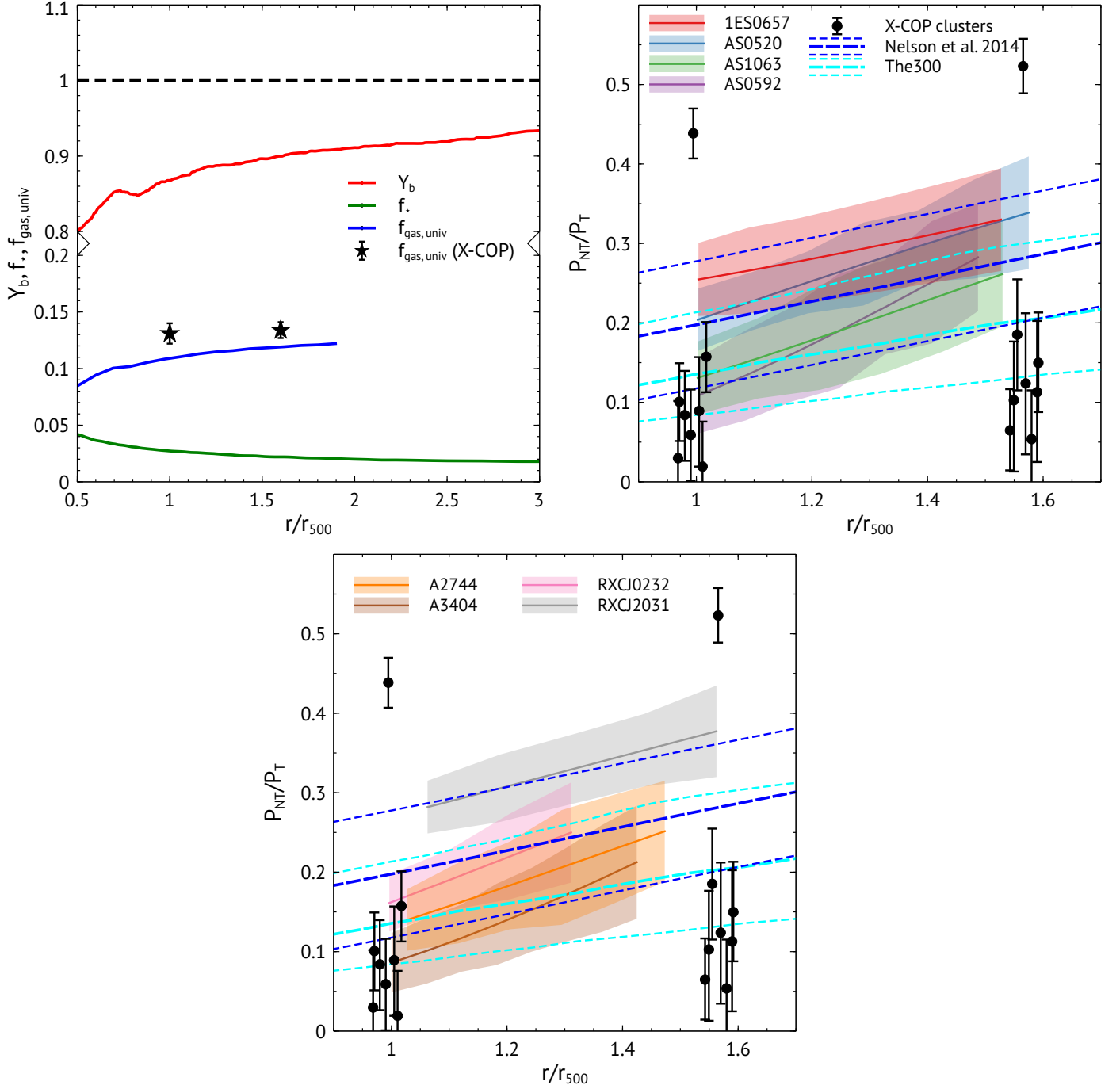


Figure 4. *Top Left:* baryon depletion factor (red), stellar fraction (green) profiles as obtained from (Angelinelli et al. 2022). Blue curve shows the universal gas fraction. Black star represents universal gas fraction used for X-COP sample. *Top Right:* Non-thermal pressure fraction profiles for 1ES0657, AS0520, AS1063, and AS0592. The blue and cyan dashed curves show the non-thermal pressure fractions predicted from the numerical simulations of Nelson et al. (2014) and Eckert et al. (2019), respectively with their 1σ uncertainties. The black data points show the non-thermal pressure obtained for X-COP sample of clusters. *Bottom:* Similar to *Top Right*, but for A2744, A3404, RXCJ0232, and RXCJ2031 clusters.

Equation 12 yields,

$$M_{\text{tot}}(< r) = M_{\text{HSE}}(< r) + \alpha(r)M_{\text{tot}}(< r) - \frac{P_{\text{th}}r^2}{(1-\alpha)\rho_{\text{gas}}G} \frac{d\alpha}{dr}, \quad (13)$$

Finally, using the formulation of enclosed gas fraction, $f_{\text{gas}}(< r) = M_{\text{gas}}(< r)/M_{\text{tot}}(< r)$, the equation 13 can be simplified as -

$$M_{\text{HSE}}(< r) = \frac{P_{\text{th}}r^2}{(1-\alpha)\rho_{\text{gas}}G} \frac{d\alpha}{dr} \left[1 - \frac{f_{\text{gas,HSE}}(1-\alpha)}{f_{\text{gas}}} \right]^{-1} \quad (14)$$

Therefore, by knowing the true gas fraction (f_{gas}) and by comparing $f_{\text{gas,HSE}}$, with the universal gas fraction, one can estimate the non-thermal pressure fraction, $\alpha(r)$, from Equation 14 (Eckert et al. 2019).

We adopt a functional form of non-thermal pressure fraction introduced by Nelson et al. (2014),

$$\alpha(r) = 1 - A \left(1 + \exp \left[-\frac{(r/R_{200})^\gamma}{B^\gamma} \right] \right) \quad (15)$$

where A , B , γ are the free parameters. For each cluster, we fix the $f_{\text{gas,HSE}}$ to the measured values (Figure 3), and f_{gas} to the universal gas fractions, as derived in Section 4.1. We vary A , B , and γ in Equation 15 iteratively until Equation 14 converges to the measured M_{HSE} values. Figure 4 shows the resulting non-thermal pressure fraction profiles of individual clusters between $0.75 < r/R_{500} < 2R_{500}$ radial range. Our measured non-thermal pressure fraction profiles show good agreement with that of hydrodynamical simulations done by Nelson et al. (2014), and The300 simulations shown in Eckert et al. (2019).

We further compare our results with the X-COP sample, as illustrated in Figure 4. Specifically, at the radius R_{500} , our measurements align with those from X-COP within 1σ uncertainties for 7 out of 8 clusters, taking into account the spread observed in their sample (excluding A2319). The non-thermal pressure fraction ($P_{\text{NT}}/P_{\text{T}}$) exhibits a range of 8–23% (median: $12.5 \pm 6\%$) at R_{500} , with RXCJ2031 showing the highest value of $23 \pm 2.2\%$. (Eckert et al. 2019) measured a median non-thermal pressure of $5.9_{-3.3}^{+2.9}\%$ for $z < 0.1$ clusters, consistent with our measurement. Compared to the X-COP sample, our selected SPT clusters demonstrate a steeper increase in $P_{\text{NT}}/P_{\text{T}}$ between the radii R_{500} and R_{200} . This discrepancy becomes more pronounced at R_{200} , where the non-thermal pressure fractions for the SPT clusters are relatively larger than those observed in the X-COP sample (though still overlaps for few clusters). This disparity may be attributed to our adoption of Y_{b} profile from (Angelinelli et al. 2022). Our measurement of $P_{\text{NT}}/P_{\text{T}}$ ranges between 21–30% at R_{200} , with

a median of $25 \pm 4\%$. We note that the determination of non-thermal pressure at the cluster outskirts using this method relies significantly on the simulated profiles of Y_{b} and f_{\star} .

Next, we determine the total mass of each cluster in our sample using Equation 12 and the derived $P_{\text{NT}}/P_{\text{T}}$. The recovered total masses are listed in Table A. We then compare our recovered masses with those measured from weak-lensing (WL) observations. Since WL mass measurements are not biased by non-thermal pressure, they provide a true estimate of the cluster mass. However, not all clusters in our sample have WL mass measurements. Only four clusters—A2744 (Medezinski et al. 2016), AS0520 (Menanteau & Hughes 2009), 1ES 0657-56 (Bradač et al. 2006), and AS1063 (Gruen et al. 2014)—have masses measured using WL. As shown in Table A, our recovered total masses are consistent with the WL masses, demonstrating the robustness of our measurements.

The ICM of dynamically active galaxy clusters experiences turbulence and bulk motion, increasing the non-thermal pressure fraction. Using high-resolution hydrodynamical simulations of 65 galaxy clusters, Nelson et al. (2014) found a strong correlation between a cluster’s dynamical state and its non-thermal pressure fraction, with the mass accretion rate as an indicator. Similarly, using centroid shift as a dynamical state indicator, we find that the non-thermal pressure fraction at R_{500} increases with centroid shift, as shown in Figure 5. This suggests that dynamically active clusters have more turbulent ICM than relaxed ones, consistent with simulations. Even with large 1σ uncertainties, our results hint a similar trend at R_{200} , as seen in Figure 5. Future X-ray missions like NewAthena may better constrain non-thermal pressure fractions at R_{200} .

5. SYSTEMATIC UNCERTAINTIES

We discuss different sources that can introduce systematic uncertainty in our measurements of non-thermal pressure at cluster outskirts. Systematic uncertainties in our measurements can arise from subtracting XMM-Newton quiescent particle background. Ghirardini et al. (2018) showed that residual soft-proton background remains (at $\sim 15\%$) after subtracting QPB, if the observation is impacted by severe soft-proton background. We, therefore, only include radial bins that are within R_{200} of the respective clusters to avoid including bins where count rates are dominated by soft-proton background. For all the clusters in our sample, the sky-background subtracted source count rates are a factor of ≥ 2 (i.e., $\geq 3.5\sigma$) higher than the QPB level at R_{200} , as shown in Figure 1. We also adopt a systematic uncertainty of

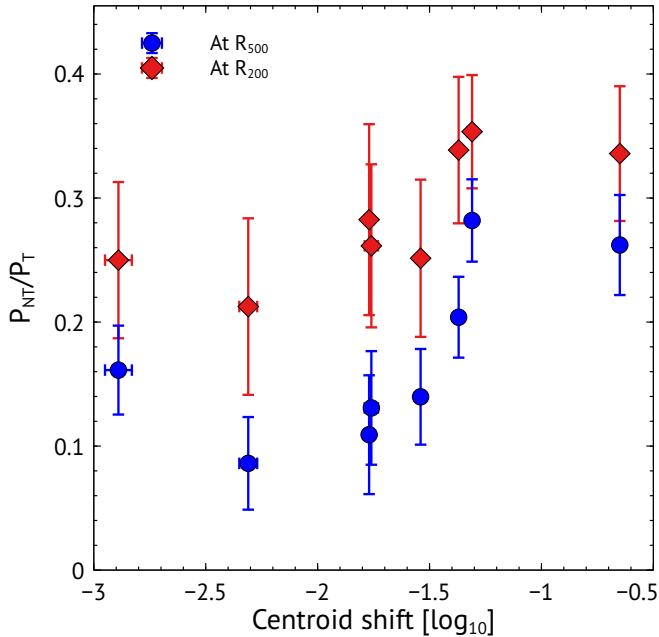


Figure 5. Non-thermal pressure fraction of galaxy clusters in our sample as a function of centroid shift. Centroid shift values have been adopted from Yuan et al. (2022). Higher centroid shift implies cluster is more dynamically active, which increases non-thermal pressure at cluster outskirts.

15% of the non X-ray background level on the measured X-ray surface brightness profiles.

Another source of systematic uncertainty may stem from our choices of simple electron temperature and density models to fit X-ray surface brightness and SZ y-map profiles. Ghirardini et al. (2019) showed that slope of density profiles steepen with radius even at larger radii, but slope of temperature profiles stay relatively flat at $r > 0.3R_{500}$. Our gNFW based density model does not capture any variation in slopes of density profiles at $r \gg r_s$, which may underestimate the uncertainty levels on density and temperature profiles at cluster outskirts.

One of major source of systematic uncertainties in non-thermal pressure measurements stem from adopted values of Y_b and f_* from hydrodynamical simulations. As seen in Figure 4, our measurements for $z > 0.1$ clusters are systematically shifted to larger P_{NT}/P_T values compared to X-COP clusters because of different choices of Y_b and f_* values between two studies.

6. CONCLUSION AND SUMMARY

X-ray observations offer a precise estimation of ICM gas density, while SZ observations provide accurate measurements of thermal pressure out to R_{200} and beyond (Ghirardini et al. 2018; Bleem et al. 2022). By integrating these complementary data sources, we can potentially enhance our understanding of cluster formation

and evolution. In this study, we have introduced a joint fitting technique that combines X-ray and SZ data to obtain precise constraints on ICM gas properties. To validate our approach, we apply this technique to a sample of 8 massive galaxy clusters ($0.16 < z < 0.35$) carefully selected from the SPT and XMM cluster catalogs. Here, we present a summary of our key findings below.

- We show that a gNFW electron density model (Amodeo et al. 2021), together with a universal temperature profile as described in Loken et al. (2002), fits best with the observed X-ray surface brightness and y -parameter profiles out to R_{200} when fitted jointly. The best-fit density and temperature profiles are in good agreement with previous other studies (e.g., Ghirardini et al. 2019, 2021; Ruppin et al. 2021).
- The pressure profiles of our cluster sample show similar trends, as expected for massive galaxy clusters ($M_{500} > 3 \times 10^{14} M_\odot$). Our measurements of pressure profiles are consistent with that of the X-COP cluster sample (Ghirardini et al. 2019) and $z > 1.2$ SPT cluster sample (Ghirardini et al. 2021). We find that the majority of the clusters in our sample show a good agreement with the baseline entropy profile between R_{500} and R_{200} , indicating that gravitational collapse governs the ICM heating in this radial range.
- Our measurements of M_{HSE} for the cluster sample range from $0.75\text{--}1.68 \times 10^{15} M_\odot$ within R_{500} and $1\text{--}2.2 \times 10^{15} M_\odot$ within R_{200} . The f_{gas} profiles of our cluster sample increase from the cluster centers and reach values between 0.108–0.148 at R_{500} and 0.144–0.165 at R_{200} .
- We adopted Y_b and f_* profiles from Magneticum simulation (Angelinelli et al. 2022) for deriving non-thermal pressure. Our estimated non-thermal pressure fraction (P_{NT}/P_T) ranges from 8% to 28% (median: $15 \pm 11\%$) at R_{500} and from 21% to 35% (median: $27 \pm 12\%$) at R_{200} , consistent with the hydrodynamical simulations (Nelson et al. 2014; Eckert et al. 2019). Our results at R_{500} are consistent with the X-COP measurements within 1σ uncertainties, but differ significantly at R_{200} . We note that our results show a steeper increase in P_{NT}/P_T between R_{500} and R_{200} compared to the X-COP sample. This disagreement likely stems from differing choices of Y_b , and f_* profiles in the two studies. We recover the total cluster mass for each cluster in our sample, accounting for non-thermal pressure, and

compare these values with masses derived from weak-lensing observations. The consistency between our recovered cluster masses and the available weak-lensing masses demonstrates the robustness of our measurements.

1 We sincerely thank the anonymous referee for their in-
 2 sightful comments and suggestions. A.S gratefully ac-
 3 knowledge support from NASA grant 80GSFC23CA045
 4 and Smithsonian Astrophysical Observatory sub-award
 5 SV2-82023. This work is based on observations obtained
 6 with the South Pole Telescope and XMM-Newton. The
 7 South Pole Telescope program is supported by the Na-
 8 tional Science Foundation (NSF) through the Grant No.
 9 OPP-1852617. XMM-Newton is an ESA science mission
 10 with instruments and contributions directly funded by
 11 ESA member states and the USA (NASA). Work at Ar-
 12 gonne National Lab is supported by UChicago Argonne
 13 LLC, Operator of Argonne National Laboratory (Ar-
 14 gonne). Argonne, a U.S. Department of Energy Office
 15 of Science Laboratory, is operated under contract no.
 16 DE-AC02-06CH11357.

REFERENCES

- Adam R., et al., 2015, *A&A*, 576, A12
- Akamatsu H., Hoshino A., Ishisaki Y., Ohashi T., Sato K., Takei Y., Ota N., 2011, *Publications of the Astronomical Society of Japan*, 63, S1019
- Amodeo S., et al., 2021, *PhRvD*, 103, 063514
- Angelinelli M., Ettori S., Dolag K., Vazza F., Ragagnin A., 2022, *A&A*, 663, L6
- Ayroulou M., Nelson D., Pillepich A., 2023, *MNRAS*,
- Babuk I., Melnyk O., Elyiv A., 2012, *Advances in Astronomy and Space Physics*, 2, 188
- Barnes D. J., Vogelsberger M., Pearce F. A., Pop A.-R., Kannan R., Cao K., Kay S. T., Hernquist L., 2021, *MNRAS*, 506, 2533
- Biffi V., et al., 2016, *ApJ*, 827, 112
- Bleem L. E., et al., 2022, *ApJS*, 258, 36
- Böhringer H., et al., 2004, *A&A*, 425, 367
- Bradač M., et al., 2006, *ApJ*, 652, 937
- Brunetti G., Jones T. W., 2014, *International Journal of Modern Physics D*, 23, 1430007
- Bulbul E., et al., 2019, *ApJ*, 871, 50
- Cavagnolo K. W., Donahue M., Voit G. M., Sun M., 2009, *ApJS*, 182, 12
- Chakraborty P., Ferland G. J., Chatzikos M., Guzmán F., Su Y., 2020a, *ApJ*, 901, 68
- Chakraborty P., Ferland G. J., Chatzikos M., Guzmán F., Su Y., 2020b, *ApJ*, 901, 69
- Coe D., et al., 2019, *ApJ*, 884, 85
- Eckert D., Roncarelli M., Ettori S., Molendi S., Vazza F., Gastaldello F., Rossetti M., 2015, *MNRAS*, 447, 2198
- Eckert D., et al., 2019, *A&A*, 621, A40
- Ettori S., et al., 2019, *A&A*, 621, A39
- Foreman-Mackey D., Hogg D. W., Lang D., Goodman J., 2013, *PASP*, 125, 306
- Ghirardini V., Ettori S., Eckert D., Molendi S., Gastaldello F., Pointecouteau E., Hurier G., Bourdin H., 2018, *A&A*, 614, A7
- Ghirardini V., et al., 2019, *A&A*, 621, A41
- Ghirardini V., et al., 2021, *ApJ*, 910, 14
- Gruen D., et al., 2014, *MNRAS*, 442, 1507
- Hitomi Collaboration et al., 2016, *Nature*, 535, 117
- Hughes J. P., Menanteau F., Sehgal N., Infante L., Barrientos F., 2009, in *American Astronomical Society Meeting Abstracts #213*. p. 448.08
- Kawaharada M., et al., 2010, *ApJ*, 714, 423
- Kéruzoré F., et al., 2020, *A&A*, 644, A93
- Kraft R., et al., 2022, *arXiv e-prints*, p. arXiv:2211.09827
- Kravtsov A. V., Nagai D., Vikhlinin A. A., 2005, *ApJ*, 625, 588

- Loken C., Norman M. L., Nelson E., Burns J., Bryan G. L., Motl P., 2002, *ApJ*, 579, 571
- Lovisari L., et al., 2020, *ApJ*, 892, 102
- Mahdavi A., Hoekstra H., Babul A., Bildfell C., Jeltema T., Henry J. P., 2013, *ApJ*, 767, 116
- Maughan B. J., Jones C., Forman W., Van Speybroeck L., 2008, *ApJS*, 174, 117
- Medezinski E., Umetsu K., Okabe N., Nonino M., Molnar S., Massey R., Dupke R., Merten J., 2016, *ApJ*, 817, 24
- Menanteau F., Hughes J. P., 2009, *ApJL*, 694, L136
- Menanteau F., et al., 2010, *ApJ*, 723, 1523
- Muñoz-Echeverría M., et al., 2023, *A&A*, 671, A28
- Nagai D., Lau E. T., 2011, *The Astrophysical Journal*, 731, L10
- Nagai D., Vikhlinin A., Kravtsov A. V., 2007, *ApJ*, 655, 98
- Nelson K., Rudd D. H., Shaw L., Nagai D., 2012, *ApJ*, 751, 121
- Nelson K., Lau E. T., Nagai D., 2014, *ApJ*, 792, 25
- Plagge T., et al., 2010, *ApJ*, 716, 1118
- Planck Collaboration et al., 2016, *A&A*, 594, A13
- Planelles S., Borgani S., Dolag K., Ettori S., Fabjan D., Murante G., Tornatore L., 2013, *MNRAS*, 431, 1487
- Pratt G. W., et al., 2010, *A&A*, 511, A85
- Pratt G. W., Arnaud M., Biviano A., Eckert D., Ettori S., Nagai D., Okabe N., Reiprich T. H., 2019, *SSRv*, 215, 25
- Rasia E., et al., 2015, *ApJL*, 813, L17
- Ruppin F., et al., 2017, *A&A*, 597, A110
- Ruppin F., McDonald M., Bleem L. E., Allen S. W., Benson B. A., Calzadilla M., Khullar G., Floyd B., 2021, *ApJ*, 918, 43
- Sarazin C. L., 1988, X-ray emission from clusters of galaxies
- Sarkar A., Su Y., Randall S., Gastaldello F., Trierweiler I., White R., Kraft R., Miller E., 2021, *MNRAS*, 501, 3767
- Sarkar A., Su Y., Truong N., Randall S., Mernier F., Gastaldello F., Biffi V., Kraft R., 2022a, *MNRAS*, 516, 3068
- Sarkar A., et al., 2022b, *ApJL*, 935, L23
- Sarkar A., et al., 2023, *ApJ*, 944, 132
- Schellenberger G., et al., 2023, *arXiv e-prints*, p. arXiv:2307.01259
- Sembolini F., et al., 2016, *MNRAS*, 457, 4063
- Shi X., Komatsu E., Nagai D., Lau E. T., 2016, *MNRAS*, 455, 2936
- Smith G. P., et al., 2016, *MNRAS*, 456, L74
- Snowden S. L., Mushotzky R. F., Kuntz K. D., Davis D. S., 2008, *A&A*, 478, 615
- Staniszewski Z., et al., 2009, *ApJ*, 701, 32
- Su Y., Buote D., Gastaldello F., Brighenti F., 2015, *ApJ*, 805, 104
- Sunyaev R. A., Zeldovich Y. B., 1972, *Comments on Astrophysics and Space Physics*, 4, 173
- Sunyaev R. A., Zeldovich I. B., 1980, *ARA&A*, 18, 537
- Truong N., et al., 2023, *arXiv e-prints*, p. arXiv:2307.01277
- Vikhlinin A., Kravtsov A., Forman W., Jones C., Markevitch M., Murray S. S., Speybroeck L. V., 2006, *The Astrophysical Journal*, 640, 691
- Voit G. M., Kay S. T., Bryan G. L., 2005, *MNRAS*, 364, 909
- Walker S., et al., 2019, *SSRv*, 215, 7
- XRISM Collaboration 2025, *arXiv e-prints*, p. arXiv:2501.05514
- XRISM Science Team 2020, *arXiv e-prints*, p. arXiv:2003.04962
- Yuan Z. S., Han J. L., Wen Z. L., 2022, *MNRAS*, 513, 3013
- Zhang Y. Y., Böhringer H., Finoguenov A., Ikebe Y., Matsushita K., Schuecker P., Guzzo L., Collins C. A., 2006, *A&A*, 456, 55
- von der Linden A., et al., 2014, *MNRAS*, 443, 1973

APPENDIX

A. PHYSICAL PROPERTIES OF OUR SAMPLE OF CLUSTERS

Cluster	$M_{\text{HSE},500}$ ($10^{15} M_{\odot}$)	$M_{\text{HSE},200}$ ($10^{15} M_{\odot}$)	$f_{\text{gas},500}$	$f_{\text{gas},200}$	$\frac{P_{\text{NT}}}{P_{\text{T}}}$ ₅₀₀ (%)	$\frac{P_{\text{NT}}}{P_{\text{T}}}$ ₂₀₀ (%)	$M_{\text{recovered},200}$ ($10^{15} M_{\odot}$)	M_{WL} ($10^{15} M_{\odot}$)
A2744	1.45 ± 0.06	1.76 ± 0.18	0.111 ± 0.005	0.153 ± 0.011	13.9 ± 3.8	25.1 ± 6.3	2.22 ± 0.63	2.1 ± 0.4^a
A3404	1.04 ± 0.07	1.21 ± 0.16	0.108 ± 0.006	0.144 ± 0.010	8.6 ± 3.7	21.2 ± 7.1	1.31 ± 0.47	–
AS0520	0.92 ± 0.08	1.37 ± 0.15	0.131 ± 0.005	0.163 ± 0.009	20.4 ± 3.3	33.8 ± 5.9	2.13 ± 0.44	1.7^b
AS0592	0.96 ± 0.06	1.12 ± 0.13	0.120 ± 0.007	0.161 ± 0.012	10.9 ± 4.7	28.3 ± 7.7	1.51 ± 0.45	–
AS1063	1.63 ± 0.07	2.13 ± 0.26	0.121 ± 0.006	0.147 ± 0.010	13.1 ± 4.6	26.1 ± 6.6	2.63 ± 0.65	2.3 ± 0.4^d
1ES 0657–56	1.68 ± 0.11	2.23 ± 0.38	0.148 ± 0.007	0.164 ± 0.012	25.4 ± 5.0	34.2 ± 8.5	3.15 ± 0.71	3.1 ± 0.5^c
RXCJ0232.2–4420	0.94 ± 0.06	1.11 ± 0.18	0.124 ± 0.005	0.149 ± 0.009	16.1 ± 3.6	24.9 ± 6.3	1.33 ± 0.43	–
RXCJ2031.8–4037	0.75 ± 0.07	1.02 ± 0.14	0.139 ± 0.005	0.165 ± 0.009	28.2 ± 3.3	35.3 ± 5.5	1.74 ± 0.47	–

Table 2. Galaxy cluster sample adopted for this study. $\frac{P_{\text{NT}}}{P_{\text{T}}}$ ₅₀₀ and $\frac{P_{\text{NT}}}{P_{\text{T}}}$ ₂₀₀ are non-thermal pressure fractions at R_{500} and R_{200} , respectively. $M_{\text{recovered},200}$ is the recovered cluster total mass after accounting for non-thermal pressure. M_{WL} represents cluster mass measured from weak-lensing (WL) observations within R_{200} adopted from: ^a Medezinski et al. (2016), ^b Menanteau & Hughes (2009), ^c Bradač et al. (2006), ^d Gruen et al. (2014).

B. BEST-FIT PARAMETERS FROM SZ Y-MAP + X-RAY SURFACE BRIGHTNESS FITTING

Cluster	$\log\left(\frac{n_0}{E(z)^2}\right)$	α	β	γ	r_s (Mpc)	T_0 (keV)	r_c (Mpc)	δ
A2744	–2.53	2.0	2.45	0.13	0.54	14.9	4.5	2.55
A3404	–2.46	1.44	2.8	0.12	0.60	16.8	2.8	2.6
AS0520	–2.71	1.41	3.3	0.11	1.0	11.8	2.6	1.64
AS0592	–1.98	0.88	3.1	0.0	0.61	13.5	2.7	2.6
AS1063	–2.04	1.9	2.3	0.11	0.29	17.9	2.0	1.2
1ES 0657–56	–2.16	1.41	3.5	0.0	0.70	15.8	2.8	1.64
RXCJ0232.2–4420	–2.25	1.2	2.36	0.45	0.41	14.4	1.6	1.3
RXCJ2031.8–4037	–2.02	1.1	2.4	0.12	0.30	9.4	1.3	0.75

C. TEMPERATURES FROM X-RAY SPECTRAL FIT ($T_{\text{X-RAY}}$) VS. OUR MEASUREMENTS OF $T_{\text{X-RAY}+\text{SZ}}$

In this section, we compare the global projected temperatures of the galaxy clusters in our sample, measured using Chandra and XMM-Newton spectral fitting ($T_{\text{X-ray}}$), with our global temperature measurements obtained from X-ray + SZ joint fitting. First, we project the best-fit 3D temperature profiles (Figure 2) onto the sky plane, following Sarkar et al. (2021) and assuming a spherical distribution,

$$T_{\text{X-ray}+\text{SZ}} = \frac{\int n_e^2 T_e^{\frac{1}{4}} dV}{\int n_e^2 T_e^{-\frac{3}{4}} dV}, \quad (\text{C1})$$

where T_e and n_e are the best-fit 3D temperature and density profiles. Finally we measure average projected temperature of the cluster within $0.15R_{500}$ – R_{200} . Figure 6 compares the resulting average projected temperatures with the global temperatures measured using spectral fit from Chandra (left) and XMM-Newton (right) observations. Our temperature measurements using joint X-ray and SZ observations more closely align with the XMM-Newton measurements than that of Chandra.

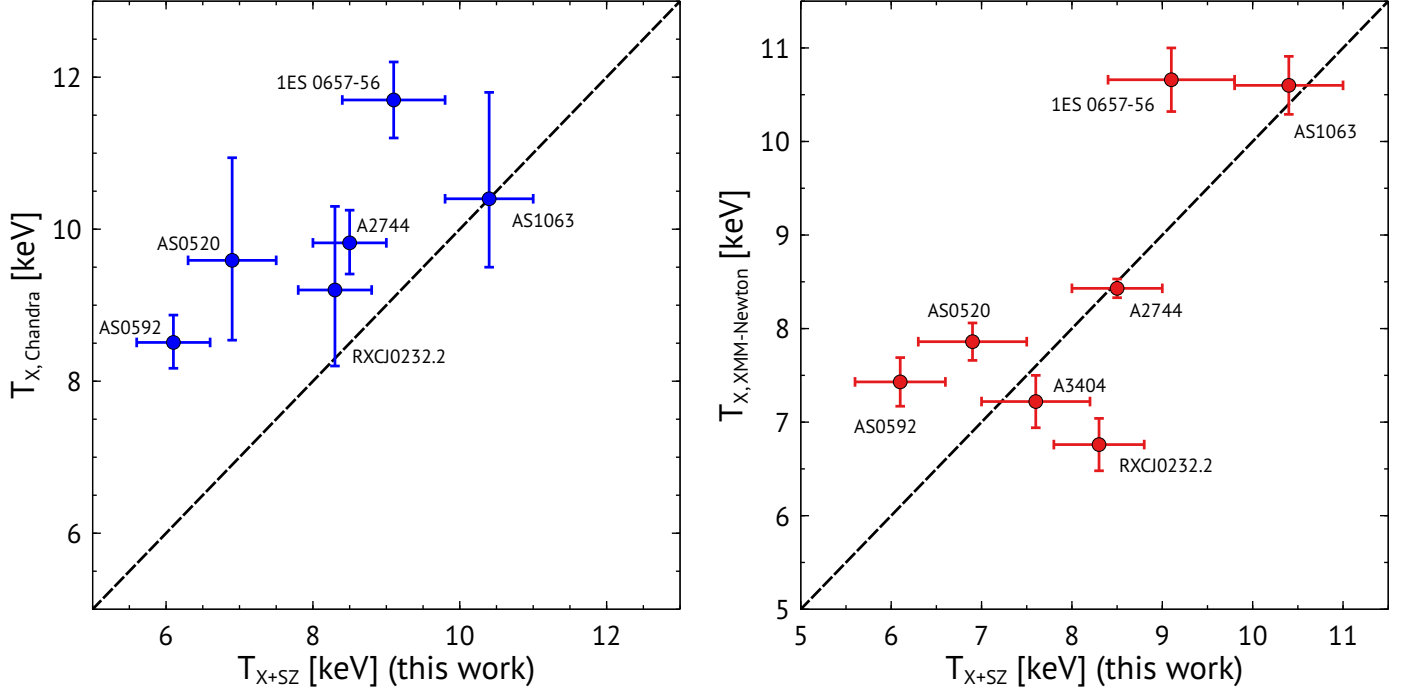


Figure 6. Comparison of global projected temperatures within $0.15R_{500} < r < R_{200}$ of clusters in our sample measured using spectral fitting with the projected temperatures within same radial range from our X-ray + SZ joint fitting. *Left:* X-ray temperatures are measured using Chandra observations and are taken from [Babyk et al. \(2012\)](#) (A2744), [Menanteau et al. \(2010\)](#) (AS0520, AS0592), and [Maughan et al. \(2008\)](#) (AS1063, 1ES 0657-56, RXCJ2032.2-4420). *Right:* X-ray temperatures are measured using XMM-Newton observations and are taken from [Lovisari et al. \(2020\)](#).